iScience

CellPress

Article

Bioprinted 3D Primary Human Intestinal Tissues Model Aspects of Native Physiology and ADME/Tox Functions

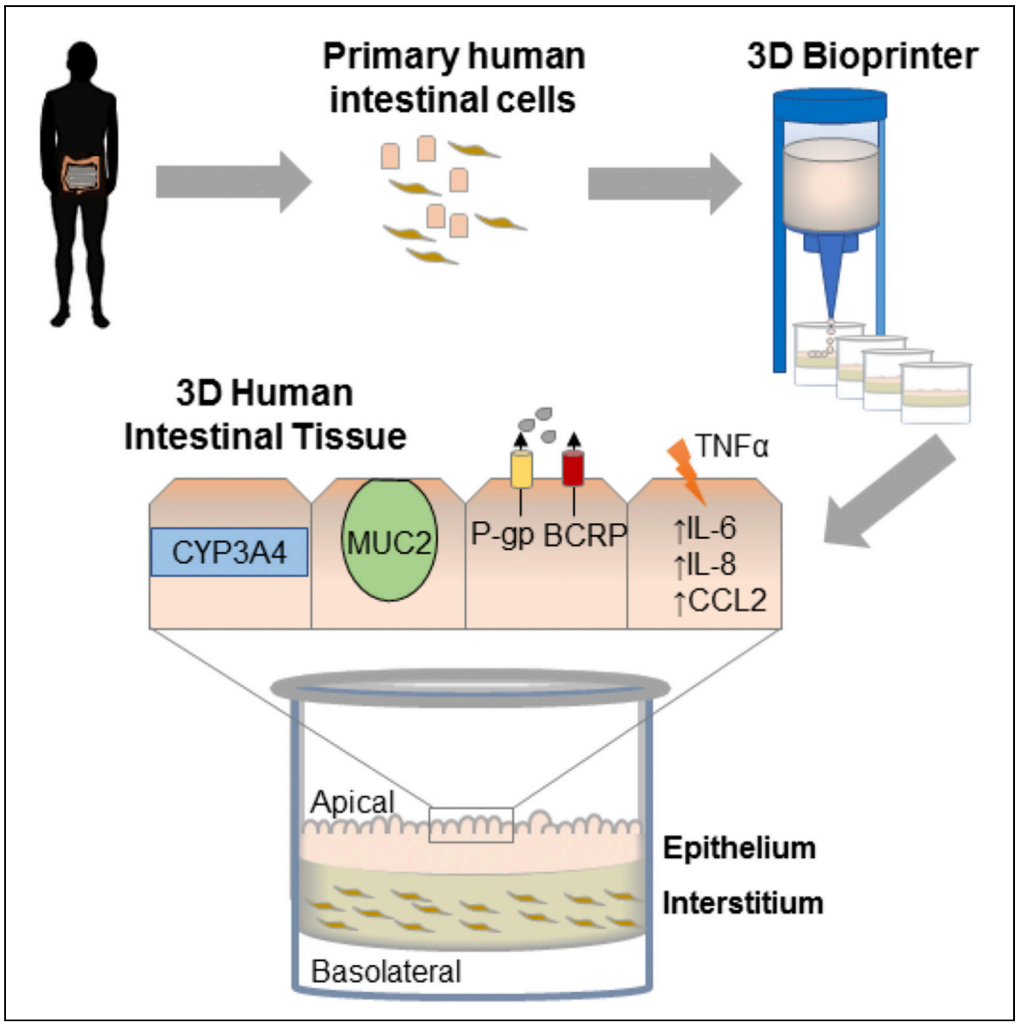

Lauran R. Madden, Theresa V. Nguyen, Salvador Garcia-Mojica, ..., Sharon C. Presnell, Deborah G. Nguyen, Kelsey N. Retting

kretting@organovo.com

HIGHLIGHTS

Bioprinted 3D human intestinal tissues enable complex modeling of ADME/Tox *in vitro*

3D intestinal tissues develop barrier function and polarized transporter expression

Key cytochrome P450 enzymes are expressed, metabolically active, and inducible

GI toxicants can trigger barrier disruption and cytotoxicity in 3D intestinal tissues

Madden et al., iScience 2, 156–167
April 27, 2018
https://doi.org/10.1016/j.isci.2018.03.015

iScience

CellPress

Article

Bioprinted 3D Primary Human Intestinal Tissues Model Aspects of Native Physiology and ADME/Tox Functions

Lauran R. Madden,[1] Theresa V. Nguyen,[2] Salvador Garcia-Mojica,[1] Vishal Shah,[1] Alex V. Le,[1] Andrea Peier,[3] Richard Visconti,[3] Eric M. Parker,[3] Sharon C. Presnell,[1] Deborah G. Nguyen,[1] and Kelsey N. Retting[1,4,*]

SUMMARY

The human intestinal mucosa is a critical site for absorption, distribution, metabolism, and excretion (ADME)/Tox studies in drug development and is difficult to recapitulate *in vitro*. Using bioprinting, we generated three-dimensional (3D) intestinal tissue composed of human primary intestinal epithelial cells and myofibroblasts with architecture and function to model the native intestine. The 3D intestinal tissue demonstrates a polarized epithelium with tight junctions and specialized epithelial cell types and expresses functional and inducible CYP450 enzymes. The 3D intestinal tissues develop physiological barrier function, distinguish between high- and low-permeability compounds, and have functional P-gp and BCRP transporters. Biochemical and histological characterization demonstrate that 3D intestinal tissues can generate an injury response to compound-induced toxicity and inflammation. This model is compatible with existing preclinical assays and may be implemented as an additional bridge to clinical trials by enhancing safety and efficacy prediction in drug development.

INTRODUCTION

Systemic availability, diminished efficacy, and off-target effects remain challenges to the successful clinical prediction of candidate drugs and contribute to attrition in drug development, highlighting the need for better preclinical tools to model intestinal function *in vitro* (Alqahtani et al., 2013; Jones et al., 2016; Peters et al., 2016). Oral delivery is the most common method for drug administration, and in addition to absorption and first-pass metabolism, the intestine serves directly as a site of off-target toxicity for compounds such as non-steroidal anti-inflammatory drugs (NSAIDs) (Boelsterli et al., 2013) and chemotherapeutic agents (Aprile et al., 2015) and indirectly as a site of drug-drug interactions (Bentz et al., 2013; Peters et al., 2016). Animal models are frequently used to estimate compound bioavailability; however, species differences can lead to disparity in the expression of metabolic enzymes and transporters, resulting in poor clinical prediction (Jones et al., 2016; Musther et al., 2014; Peters et al., 2016). Human intestinal slices can provide correct cellular architecture and physiological complexity; however, limited viability *ex vivo* (about 24 hr) and incompatibility with cryopreservation restrict use to short-term studies (Li et al., 2016). Predominant *in vitro* systems used to study intestinal bioavailability and toxicity include intestinal microsomes and two-dimensional (2D) monolayers. Microsomes are a convenient tool for initial assessment of metabolism, but cannot model cellular level outcomes. Physiological conditions lacking in 2D culture may be improved by microfluidic chip models; however, maintenance of cell-cell and cell-matrix interactions and scale-up for high-throughput applications remain challenging (Bhatia and Ingber, 2014; Chi et al., 2016). Standard 2D monolayers and more recent gut-on-a-chip systems commonly include cell lines originating from colorectal and duodenal tumor tissue (Alqahtani et al., 2013; Kim et al., 2012) that may exhibit altered metabolic profiles and expression patterns of xenobiotic-metabolizing enzymes and transporters potentially leading to misrepresentation of the native response (Prueksaritanont et al., 1996; Yamaura et al., 2016). The colorectal tumor-derived Caco-2 cell line is the most established model to study permeability and predict intestinal absorption. Known limitations of the Caco-2 model include reduced CYP450 activity (Prueksaritanont et al., 1996; Yamaura et al., 2016), variability with passage number, and inconsistencies between subclones of the cell line (Bentz et al., 2013).

Limitations of common *in vitro* models have sparked the development of methods utilizing primary human intestinal cells. Although primary monocultures more closely resemble *in vivo* tissue compared with cell lines (Kauffman et al., 2013; Takenaka et al., 2016), separation of the epithelium from supportive cells

[1]Organovo, Inc., San Diego, CA 92121, USA

[2]Department of Pharmacokinetics, Merck & Co., Inc., Rahway, NJ 07065, USA

[3]Department of Pharmacology, Merck & Co., Inc., Kenilworth, NJ 07033, USA

[4]Lead Contact

*Correspondence: kretting@organovo.com

https://doi.org/10.1016/j.isci.2018.03.015

may impair function and limit the ability to study complex cell interactions including interplay with interstitial cells or inflammatory responses. The discovery of organoids to expand primary cells (Sato et al., 2011; Yin et al., 2014) or differentiate pluripotent stem cells (Kauffman et al., 2013; Watson et al., 2014) revealed another path to model the intestine *in vitro*. Organoids derived from all regions of the intestinal tract (Wang et al., 2015) can be applied to intestinal research including organ development, disease modeling, and regenerative medicine (Fatehullah et al., 2016; Sinagoga and Wells, 2015), although they may lack *in vivo* organ physiology. Notably, the closed lumen of the organoid structure with inward epithelial orientation makes the apical surface relatively inaccessible for absorption, distribution, metabolism, and excretion (ADME) assays. Approaches to create accessible compartments can require a complex bioreactor setup (Schweinlin et al., 2016) and produce monolayers with non-physiological transepithelial electrical resistance (TEER) (Kauffman et al., 2013; VanDussen et al., 2015). Cell-seeded engineered three-dimensional (3D) tubular scaffolds have recently been utilized with hollow lumens to promote a more native-like microenvironment (Chen et al., 2017); however, functional characterization is restricted to the apical compartment by geometry, making most standard ADME/Tox assays that require access to both apical and basal compartments incompatible.

To overcome existing limitations of the current *in vitro* systems, a proprietary bioprinting platform was utilized to develop a multicellular 3D primary human intestinal tissue model to better mimic native tissue structure and function (Nguyen et al., 2016; King et al., 2017). The fully human primary cell-derived tissue designed with laminar architecture incorporates a polarized intestinal epithelium supported by an interstitial tissue layer allowing compatibility with standard histological and biochemical ADME/Tox readouts. Tissues maintained viability over 2 weeks in culture, developed barrier function, and demonstrated selective permeability. Presence of functional key CYP450 metabolic enzymes and transporters was confirmed with endogenous expression similar to native intestine. Last, tissue injury was evaluated in response to known toxicants indomethacin and tumor necrosis factor alpha (TNF-α) revealing barrier disruption and cytotoxicity at the biochemical and histological levels. The human tissue combined with the reproducibility of the automated 3D bioprinting platform and compatibility with standard assay approaches make this system a practical *in vitro* tool for ADME/Tox applications across drug development.

RESULTS

Histological Characterization of 3D Human Intestinal Tissue

The Organovo 3D NovoGen Bioprinter system was used to create an *in vitro* model of the human intestine. The tissue was generated with bilayered architecture, consisting of a human intestinal myofibroblast (IMF) interstitium supporting an epithelial layer containing human intestinal epithelial cells (hIEC) and maintained up to 21 days in culture. Tissues were printed on cell culture inserts (Figure 1A) allowing access to both apical and basolateral surfaces for direct compound testing. Histological analysis at day 17 showed that tissues exhibited polarized columnar epithelial morphology and secondary structure formation (Figures 1B–1I). The epithelial and interstitial tissue compartments are in direct contact with each other but remained distinct, with correct expression of epithelial (CK19) and myofibroblast (vimentin) cell-specific markers (Figure 1C). E-cadherin and ZO-1, key proteins involved in tight junction formation and barrier function, were expressed between epithelial cells of the hIEC layer (Figure 1D). Correct polarization of the hIEC and brush border formation were seen by positive staining for brush border protein villin at the apical surface (Figure 1E). Periodic acid-Schiff (PAS)/Alcian blue staining confirmed an apical brush border and suggested the presence of a subpopulation of goblet cells as well as the excretion of mucus (Figure 1F). Immunohistochemistry for mucin-2 confirmed the presence of goblet cells and mucous secretion (Figure 1G), a feature similar to native tissue and an indication of normal intestinal function. In addition to goblet cells, other specialized cell types present in the intestinal epithelium included lysozyme-positive Paneth cells and chromogranin-expressing enteroendocrine cells (Figures 1H and 1I). Patterning of 3D intestinal tissues was similar to that observed in native intestinal tissue and consistent between multiple donors (Figure S1). Tissue architecture of the 3D intestinal model was also compared with that of standard Caco-2 monolayer culture (Figure S2). Caco-2 monolayers achieved a polarized epithelial phenotype with tight junction formation, although epithelial morphology appeared less columnar and lacked secondary structure formation. Subpopulations of specialized cells and evidence of mucus production were also absent in Caco-2 monolayers (Figure S2). Substitution of hIEC with Caco-2 cells in the 3D bioprinted model produced a bilayered structure with increased thickening of the epithelial layer and cyst formation over time, akin to the cancer origin (Figure S3A). However, this phenotype change did not improve transporter or enzyme gene expression to the level of 3D intestinal tissues fabricated with primary hIECs (Figure S3B).

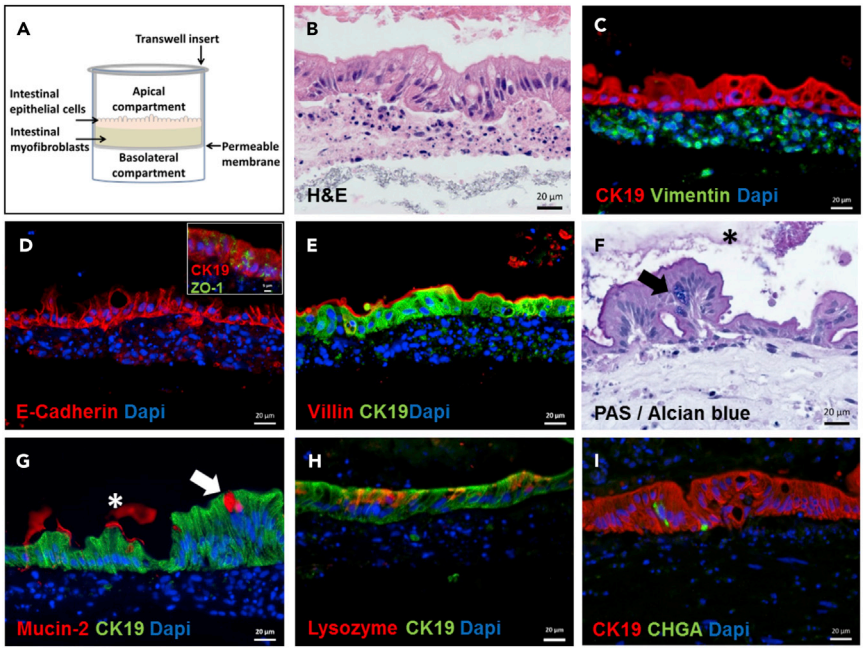

Figure 1. Architecture of 3D Intestinal Tissue

(A) A bilayered architecture is achieved by bioprinting an interstitial layer containing adult human intestinal myofibroblasts (IMF) followed by adult human intestinal epithelial cells (hIEC). The vimentin-expressing interstitial cells and CK19-expressing epithelial compartments remain separate over 17 days in culture (B, C). Epithelial cells express markers necessary for barrier formation such as E-cadherin (D), ZO-1 (D, inset), and apically expressed villin (E). Mucus production from goblet cells (* denotes secreted mucus, arrow indicates goblet cells) is observed throughout culture (F, G). Lysozyme-stained Paneth cells (H) and chromogranin-expressing enteroendocrine cells (I) are also present.

Thus the standard Caco-2 monolayer was used as the main comparison to bioprinted tissues composed of primary hIECs.

Characterization of Gene Expression

Gene expression analysis was utilized to further evaluate the expression of key intestinal epithelial tissue markers, metabolic enzymes, and transporters in the 3D intestinal tissue and was compared with both native donor intestinal tissue and standard Caco-2 monolayers (Figure 2). Although five native donor tissues were processed, challenges in obtaining high-quality donor material resulted in the utilization of three of five donors for gene expression analysis. To specifically study differential expression in the epithelium and to remove any variance in the total cell number, genes were analyzed relative to the expression of epithelial-specific marker CK19. Heatmap visualization shows close clustering of 3D intestine to the native intestine compared with more disparate Caco-2 monolayers (Figure 2A). In support of histological findings, tight junction marker E-cadherin *(CDH1)* and brush border marker villin (*VIL1*) were highly expressed, as well as markers for specialized cell subpopulations including Paneth cells (*LYZ*), enteroendocrine cells (*CHGA*), and goblet cells (*MUC2*) (Figure 2B). Key xenobiotic-activated nuclear receptors involved in drug metabolism and disposition including *VDR, PXR (NR1I2)*, and *CXR (NR1I3)* were expressed in 3D intestinal tissue at comparable levels to native intestine. Major intestinal Phase I CYP450 metabolic enzymes including *CYP3A4, CYP2C9, CYP2C19, CYP2D6,* and *CYP2J2* were also detected. Clinically important *CYP3A4* was highly expressed in the 3D intestinal model, whereas it was notably not detectable in Caco-2 monolayers (Figure 2B). Key intestinal Phase II metabolic enzymes *GSTP1* and *UGT1A1* were expressed, as well as regulators of fatty acid metabolism, including *DGAT1, MOGAT2,* and *MTTP*. Major efflux transporters *P-gp (ABCB1, MDR1)* and *BCRP (ABCG2)*, key uptake transporters *PEPT1 (SLC15A1)* and *OATP2B1 (SLCO2B1)*, and intestinal bile acid-related transporters *ASBT (SLC10A2), OSTa (SLC51A),* and *OSTb (SLC51B)* were expressed in 3D intestinal tissues with levels comparable with those in native intestine (Figure 2B). Collectively, gene expression levels in 3D intestinal tissues corresponded to endogenous levels observed in native tissue, whereas Caco-2 monolayers exhibited reduced, overexpressed, or absent expression of several genes suggesting that the bioprinted model more closely resembles native tissue.

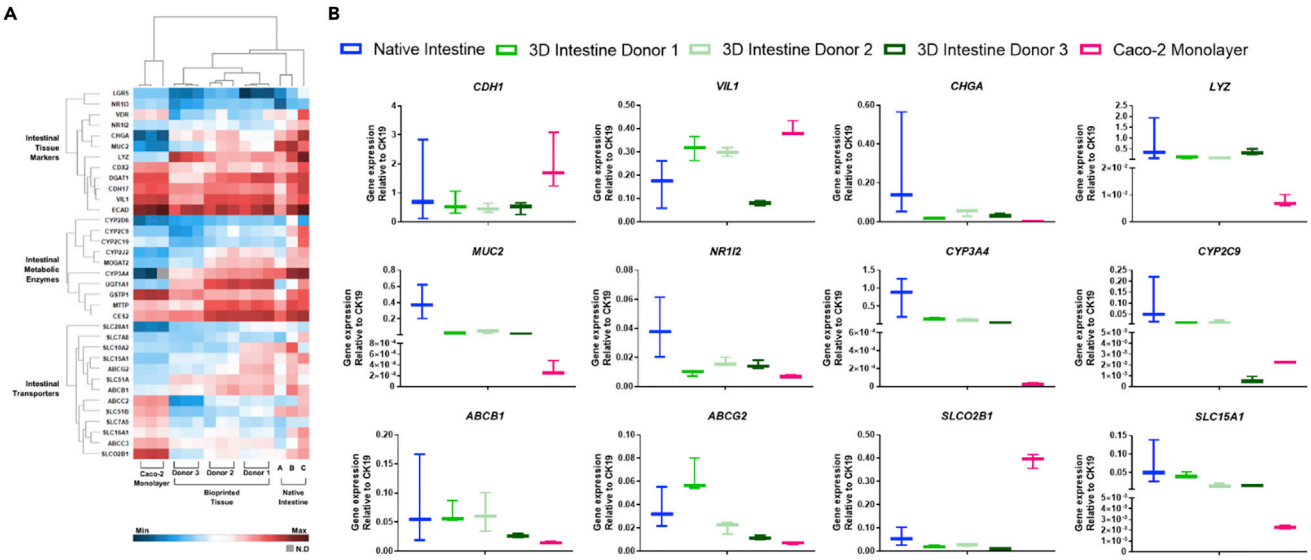

Figure 2. Gene Expression Comparisons of Native Intestine, 3D Intestinal Tissue, and Caco-2 Monolayers

(A) Heatmap clustering shows a closer relationship between native intestine and 3D intestinal tissue than Caco-2 monolayers (native intestine N = 3 donors, 3D intestine n = 3 biological replicates per donor, and Caco-2, n = 3 biological replicates).

(B) General markers for intestinal barrier function (*CDH1, VIL1*) are similar among the three groups. Epithelial subtype markers are highest for native and 3D intestinal tissue. Drug-inducible transcription factor *NR1I2* (*PXR*) is similar for native intestine and 3D intestinal tissue. Native intestine and 3D intestinal tissue express all metabolic enzymes analyzed, including Phase I cytochrome P450s, the majority of which Caco-2 cells lack. Transporters are expressed by all three groups, with variation in the level. For efflux transporters, 3D intestine is most similar to native intestine, whereas Caco-2 cells underexpress *ABCB1* (*P-gp*) and *ABCG2* (*BCRP*). Uptake transporters *SLC15A1* (*PEPT1*) and *SLCO2B1* (*OATP2B1*) are similarly expressed by native and 3D intestine, but not by Caco-2 monolayers. Data in (B) are expressed as mean ± SD.

Demonstration of Cytochrome P450 Metabolic Function in 3D Intestinal Tissue

Functional assays were performed to evaluate the activity and specificity of CYP3A4 and CYP2C9, two major intestinal Phase I cytochrome P450 metabolic enzymes profiled in gene expression studies (Figure 3). CYP2C9 activity was readily detected in 3D intestinal tissue by luminogenic P450 substrate conversion and could be significantly inhibited by sulfaphenazole (Figure 3A). CYP3A4 activity and specific inhibition by ketoconazole were confirmed by both a luminogenic P450 substrate conversion (Figure 3B) and midazolam metabolite formation (Figures 3D and 3E). Luminogenic substrate conversion occurred at a higher level in 3D intestine compared with Caco-2 monolayers (Figure 3C), and only 3D tissues were induced by rifampicin treatment (Figures 3C and 3E). Rifampicin treatment was associated with significantly higher turnover of CYP3A substrates in treated tissues and significant upregulation of PXR-inducible genes including *CYP2C9, CYP3A4, CYP3A5, P-gp*, and *UGT1A1* (Figures 3E and 3F). Variation in human CYP3A-dependent metabolism is well established (Paine et al., 1997). Comparison of CYP3A4 activity by midazolam turnover for 3D intestinal tissues fabricated from three separate donors showed expected inter-individual donor variation (Donor 1: 19.3 ± 1.9; Donor 2: 2.85 ± 0.59; Donor 3: 3.6 ± 3.6 pmol/min/mg) consistent with gene expression data (Figure 2A) as well as demonstrated reproducibility of ketoconazole inhibition and rifampicin induction between donors (Table S1). The degree of variability in CYP3A4 activity was consistent with observations of native intestine gene expression in the current study (6.3-fold among donors, Figure 2A) and with previous studies evaluating intestinal CYP3A4 activity (18-fold among donors) (Paine et al., 1997).

Demonstration of Barrier Function

The intestine is a selectively permeable barrier, regulating absorption of both nutrients and xenobiotics. TEER was utilized to measure barrier function in 3D intestinal tissues over a 21-day culture period. Measurements demonstrated that the tissues developed and maintained barrier function between days 10 and 21 of culture, exhibiting values within a physiological range (50–100 Ω*cm^2) comparable to native human intestine (Srinivasan et al., 2015) (Figure 4A). Representative compounds with high and low permeability were used to further validate 3D intestinal tissue barrier function (Figure 4B, Table S2). Paracellular transport marker lucifer yellow correctly demonstrated low permeability in 3D intestine (P_{app} = 0.45 ± 1.5 × 10^6 cm/s), suggesting the

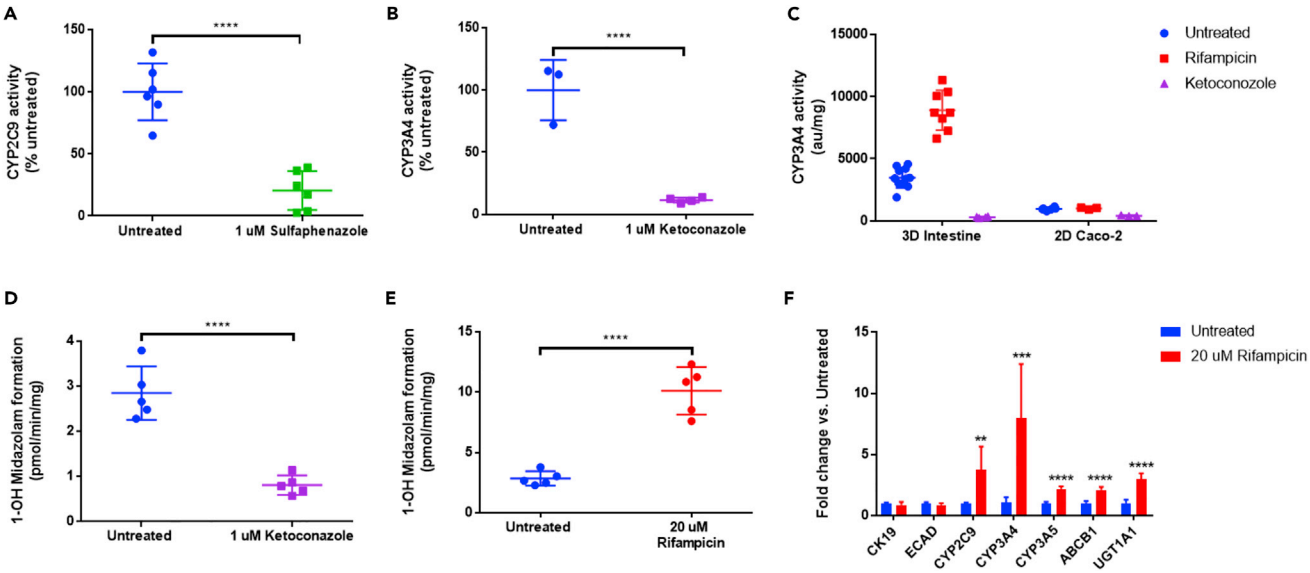

Figure 3. Cytochrome P450 Metabolism in 3D Intestinal Tissue

(A) CYP2C9 basal activity was validated by a luciferin activity assay and was reduced by inhibitor sulfaphenazole (n = 6). CYP3A4 activity was shown by luciferin activity assay (n = 3–4) (B, C) and midazolam hydroxylation (n = 5) (D, E), both of which were inhibited by ketoconazole. (C, E) CYP3A4 induction via rifampicin treatment was detected by increased luciferin activity and midazolam metabolism in 3D intestine (n = 5). (C) A comparison of CYP3A4 activity in 3D intestinal tissue with 2D Caco-2 monolayer shows low activity of CYP3A4 in Caco-2 monolayers with no rifampicin induction (n = 4–11 for 3D intestine, n = 3 for 2D Caco-2). (F) Rifampicin treatment increased gene expression of PXR-regulated CYPs, *ABCB1* (*P-gp*), and *UGT1A1* but not *CK19* and *ECAD* (n = 4). Level of significance: ****$p < 0.0001$, ***$p < 0.001$, **$p < 0.01$ by two-way ANOVA. Data are expressed as mean ± SD.

presence of an intact physical barrier for drug transport. The 3D intestinal tissues correctly distinguished between low-, intermediate-, and high-permeability compounds. Mitoxantrone (P_{app} = 0.2 ± 0.03 × 10^6 cm/s) is a low-permeability compound with absorption mainly mediated by ABCG2 (BCRP) efflux transporter. Topotecan and digoxin showed P_{app} values in the intermediate range (3.1 ± 0.63 × 10^6 cm/s and 8.53 ± 2.02 × 10^6 cm/s, respectively), whereas propranolol, a passive transcellular transport reference compound, showed the highest permeability (P_{app} = 14.8 ± 1.96 × 10^6 cm/s).

In comparison, Caco-2 monolayers demonstrated significantly higher TEER measurements (840 ± 55 Ω*cm^2) (Figure 4C). When substituted for hIEC in the 3D bioprinted model, 3D Caco-2 tissues had reduced TEER (254 ± 45 Ω*cm^2) compared with their 2D counterparts, a possible effect of cyst-like secondary structure formation, but the values remained above a physiological range. Both 2D and 3D Caco-2 models had low lucifer yellow permeability (P_{app} = 0.46 ± 0.25 × 10^6 cm/s and 1.05 ± 0.1 × 10^6 cm/s, respectively) confirming barrier formation, whereas IMF tissue alone did not show barrier function (5 ± 3 Ω*cm^2) and exhibited high permeability (163 ± 29 × 10^6 cm/s) (Figure 4D).

Transporter Localization and Function in 3D Intestinal Tissue Model

Intestinal efflux and uptake transporters can be both sites of drug-drug interactions and limiting factors for drug absorption. Immunohistochemical staining confirmed the correct polarized epithelial expression of key efflux transporters at the apical (P-gp [ABCB1], BCRP [ABCG2], MRP2 [ABCC2]) and basolateral (MRP3 [ABCC3]) surfaces in a continuous pattern similar to native intestine (Figures 5A, 5B, and S4). To assess the capability of 3D intestinal tissues to predict active efflux, P-gp and BCRP function were evaluated by measuring bidirectional transport with and without inhibition (Figures 5C and 5D). Under control conditions, asymmetric permeability of P-gp substrate digoxin was observed with an efflux ratio greater than 2. Inhibition of P-gp by zosuquidar (Dantzig et al., 1996) decreased the rate of B to A transport, reducing the efflux ratio to 1.2, to confirm the activity of P-gp. BCRP function was tested by efflux of topotecan (Figure 5D) and mitoxantrone (Figure S5). BCRP/P-gp substrate topotecan and BCRP substrate mitoxantrone were preferentially transported in the B to A direction with efflux ratios of 8.8 and 190, respectively. Furthermore, subsequent inhibition of topotecan transport by the BCRP inhibitor Ko143 (Allen et al., 2002) reduced the efflux ratio to 3.6 and dual inhibition with Ko143 and zosuquidar further decreased the

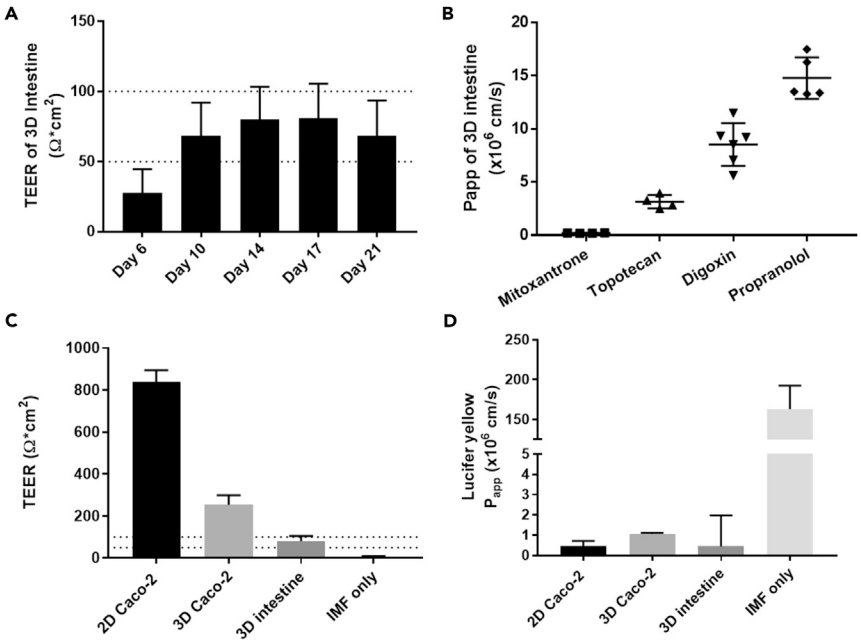

Figure 4. Barrier Function of 3D Intestinal Tissue

(A) Transepithelial electrical resistance (TEER) was measured for 3D intestinal tissue from day 6 to day 21, showing increase early in culture, with maintenance of barrier function within physiological levels (dotted lines) after day 10 (n = 24).

(B) Permeability of test compounds for 3D intestine, measured in the apical to basal direction, shows distinction between low- (mitoxantrone [n = 4]), moderate- (topotecan [n = 4], digoxin [n = 6]), and high- (propranolol [n = 5]) permeability compounds.

(C) Comparison of TEER values shows more physiological TEER values for 3D intestine (n = 24) and 3D Caco-2 (n = 6) versus 2D Caco-2 (n = 5), whereas IMF alone does not show barrier function (n = 19).

(D) Comparison of lucifer yellow permeability values between models shows low permeability for all epithelial-cell-containing models and high permeability for IMF only (n = 4 for 2D and 3D Caco-2 and IMF only, n = 28 for 3D intestine). Data are expressed as mean ± SD.

efflux ratio to 1.4. Collectively, these results demonstrate that the 3D intestinal tissue model expresses clinically relevant P-gp and BCRP transporters with proper localization and function. Compounds assessed demonstrate greater efflux ratio similarity to other models composed of primary human intestinal cells than to Caco-2 models (Table S3). Histological analysis showed apical P-gp and BCRP expression in patches across Caco-2 monolayers, whereas MRP2 and MRP3 appeared to be overexpressed (Figures 5A, 5B, and S4). Transporter expression patterning was not rescued by substitution of Caco-2 cells into the 3D bioprinted model (Figure S3).

Characterization of 3D Intestinal Tissues as a Model for Gastrointestinal Toxicity

The utility of the 3D intestinal model for compound toxicity applications was evaluated by the NSAID indomethacin, a prostaglandin E_2 (PGE2) oxygenase inhibitor and known gastrointestinal (GI) toxicant that can reduce intestinal epithelial barrier function through enterocyte apoptosis and necrosis (Boelsterli et al., 2013). The 3D intestinal tissue showed a dose-dependent decrease in barrier function as measured by TEER in response to 24-hr indomethacin treatment (Figure 6A). Injury to the intestinal cells was detected by lactate dehydrogenase (LDH) release and was significantly increased in the presence of indomethacin doses above 0.25 mM (Figure 6B), consistent with previous reports modeling indomethacin injury *in vitro* (Tang et al., 1993). All doses of indomethacin demonstrated inhibition of prostaglandin E_2 secretion, confirming the known mechanism of activity (Figure 6C). Histological analysis further illustrated dose-dependent disruption of epithelial morphology with decreased E-cadherin expression, consistent with loss in barrier function (Figure 6D). Release of inflammatory cytokines may also damage the intestine, and TNF-α is a major contributor to disease-related inflammation and intestinal toxicity (Neurath, 2014; Peyrin-Biroulet, 2010). To evaluate the susceptibility of the model to pro-inflammatory cytokines, tissues were dosed with TNF-α for 24 hr and evaluated for changes in morphology, LDH release, and gene

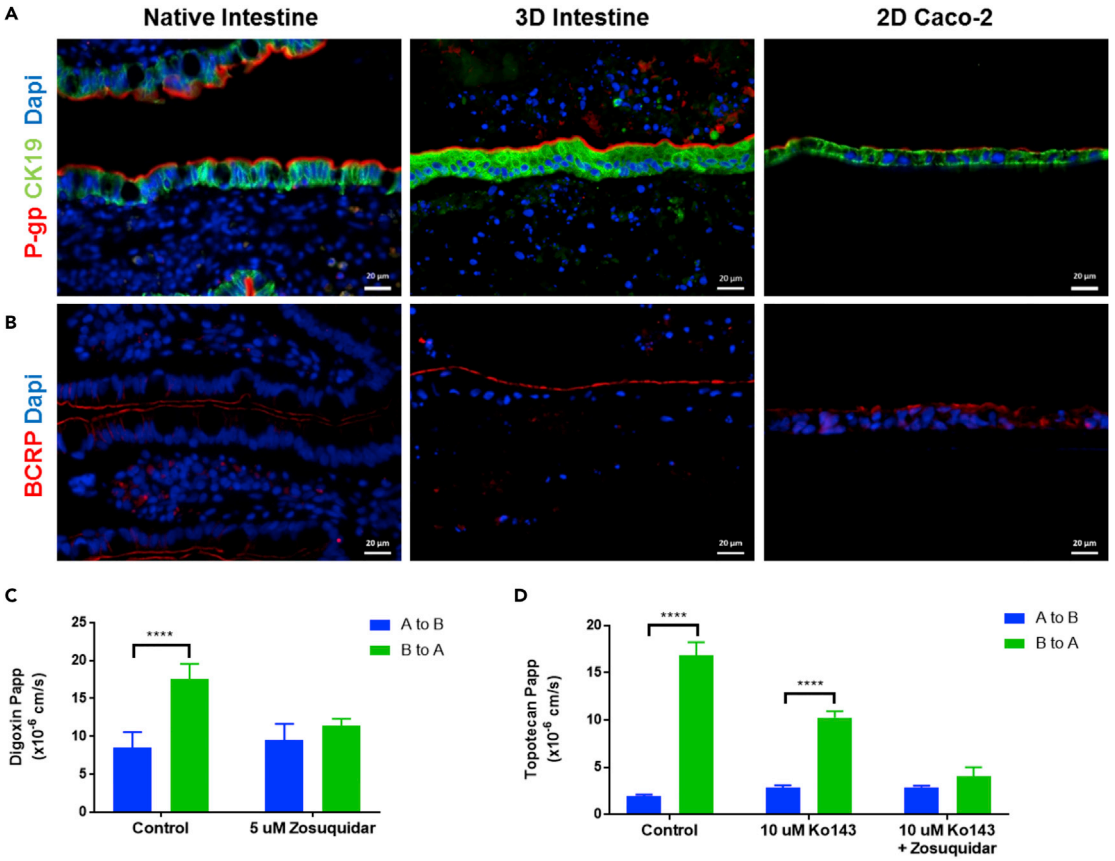

Figure 5. P-gp and BCRP Transporter Function in 3D Intestinal Tissue

(A and B) (A) P-gp and (B) BCRP are apically localized in 3D intestinal tissue, similar to native intestine. Expression in Caco-2 monolayers was in patches at the apical surface.

(C) P-gp substrate digoxin had greater permeability in the B to A direction with efflux ratio of 2.1. In the presence of P-gp inhibitor zosuquidar, the efflux ratio of digoxin reduced to 1.2 (n = 6).

(D) BCRP/P-gp substrate topotecan had an efflux ratio of 8.8 under control conditions. BCRP inhibition by Ko143 reduced B to A transport and the efflux ratio decreased to 3.6. Dual inhibition of P-gp and BCRP resulted in ablation of transport with an efflux ratio of 1.4 (n = 3–4). Level of significance: ****$p < 0.0001$ by two-way ANOVA. Data in (C) and (D) are expressed as mean ± SD.

expression (Figure 7). TNF-α altered the epithelial morphology and resulted in the dissociation of cells from the interstitial layer accompanied by a significant increase in LDH release, suggesting a cytotoxic response and enterocyte death. Gene expression for several known targets of the TNF-α/nuclear factor (NF)-κB pathway including interleukin (*IL)-6*, *IL-8*, *CCL2*, *CXCL10*, *ICAM1*, and *TNF-α* were upregulated, demonstrating activation of an inflammatory cascade (Figure 7C) in response to tissue injury.

DISCUSSION

Current preclinical models are limited in the ability to capture complexities and function of human intestinal tissue, which can lead to poor predictability in drug development (Alqahtani et al., 2013; Aprile et al., 2015; Boelsterli et al., 2013; Jones et al., 2016; Peters et al., 2016). This study incorporated primary cells into a fully human 3D bioprinted intestinal tissue model to recapitulate multiple facets of native intestinal biology and function *in vitro*. Histological analysis of the 3D intestinal tissues confirmed development and maintenance of a polarized epithelium with columnar epithelial morphology, tight junctions, and apical brush border formation. Stability of tissue architecture and function for greater than 2 weeks in culture suggests that the model may be suitable for extended compound studies.

In this study, the 3D intestinal model was compared with Caco-2 cells cultured as a standard 2D monolayer with results suggesting that the 3D tissues more closely mimic native tissue in gene and protein expression

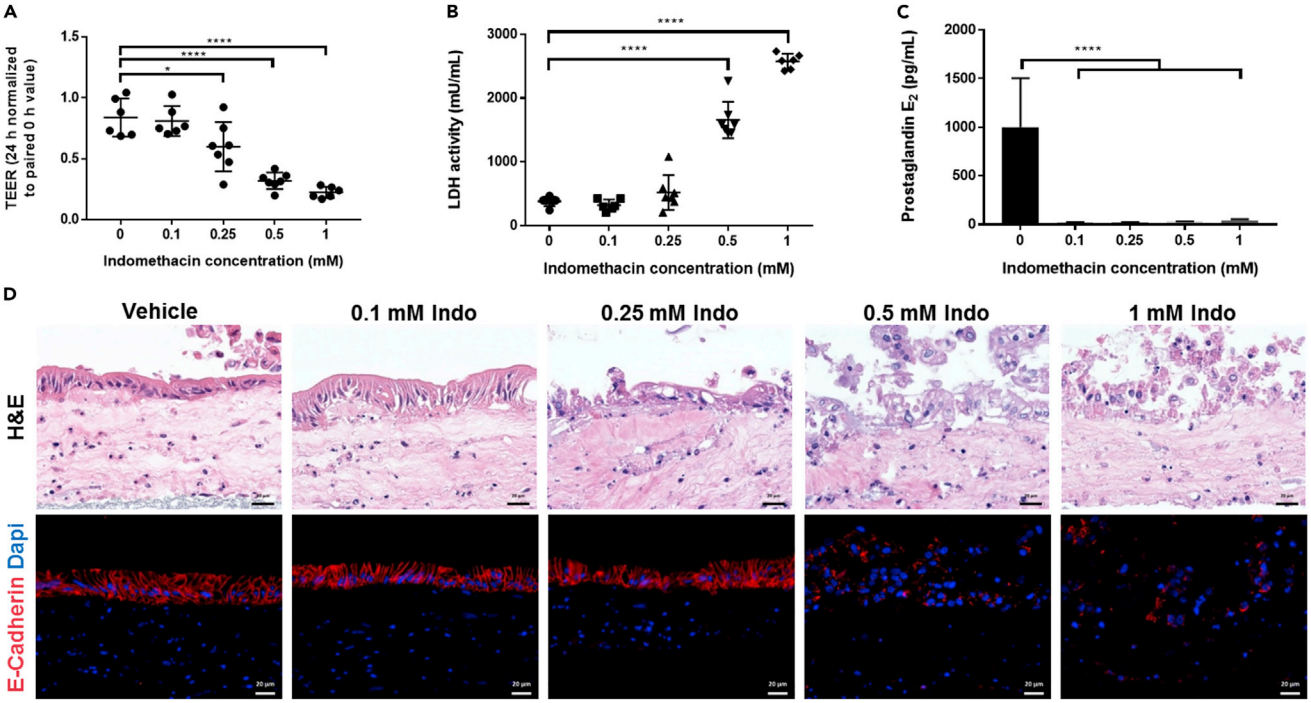

Figure 6. Indomethacin Toxicity in 3D Intestinal Tissue

(A) TEER measurements of tissues following 24-hr incubation with ethanol vehicle or varying doses of indomethacin show dose response decrease in TEER with increasing indomethacin.

(B) LDH activity increased with increasing indomethacin dose, suggesting increased cytotoxicity.

(C) Prostaglandin E_2 synthesis decreased to similar levels for all indomethacin doses tested, confirming drug activity (n = 6–7, A–C).

(D) Histology of indomethacin-treated tissues shows disruption of the epithelium and distorted nuclear staining at higher doses of indomethacin, accompanied by a reduction in E-cadherin, a marker of barrier function. Level of significance: ****$p < 0.0001$ by one-way ANOVA. Data in (A–C) are expressed as mean ± SD.

patterning and function. The divergence of Caco-2 cells from native tissue, consistent with previous reports (Prueksaritanont et al., 1996; Takenaka et al., 2014), may be due in part to their cancer origin and variability in expression patterns of metabolic enzymes and transporters along the GI tract (Paine et al., 1997; Peters et al., 2016). Both native donor tissue and the 3D intestinal model were derived from the ileum, whereas Caco-2 cells are derived from the colon. Substitution of primary intestinal epithelial cells with Caco-2 cells in the 3D system produced phenotypes more consistent with native tissue, including secondary structure formation, indicating a benefit to the 3D microenvironment that may be in part influenced by cross talk with interstitial cells, but did not rescue aberrant expression patterning.

Histology and gene expression analyses demonstrated the presence of specialized cell subpopulations in 3D intestinal tissues that are notably absent in cell lines including the Caco-2 model. The presence of mucin-2-expressing goblet cells, evidence of mucus production, and lysozyme-expressing Paneth cells suggests the potential for modeling mucosal barrier function and antimicrobial or microbiome function. Chromogranin-positive cells suggest the potential to study enteroendocrine function in the gut, including glucagon-like peptide (GLP)-1 signaling. Cell subpopulations indicate that primary cells in 3D intestinal tissues may be able to undergo directed differentiation by modification of culture conditions similar to maturation observed in organoid cell culture (Sato et al., 2011; Spence et al., 2011; Yin et al., 2014). Incorporation of induced pluripotent stem cells may be considered as an alternative cell source to primary cells, although maturity can resemble a fetal stage phenotype (Sinagoga and Wells, 2015) with inconsistent barrier function over time (Kauffman et al., 2013).

The 3D intestinal tissue demonstrated the expression and function of key enzymes involved in xenobiotic metabolism including CYP3A4, an enzyme known to be absent in Caco-2 models (Yamaura et al., 2016), consistent with our findings. Enzyme activity was confirmed by modulation of midazolam hydroxylation

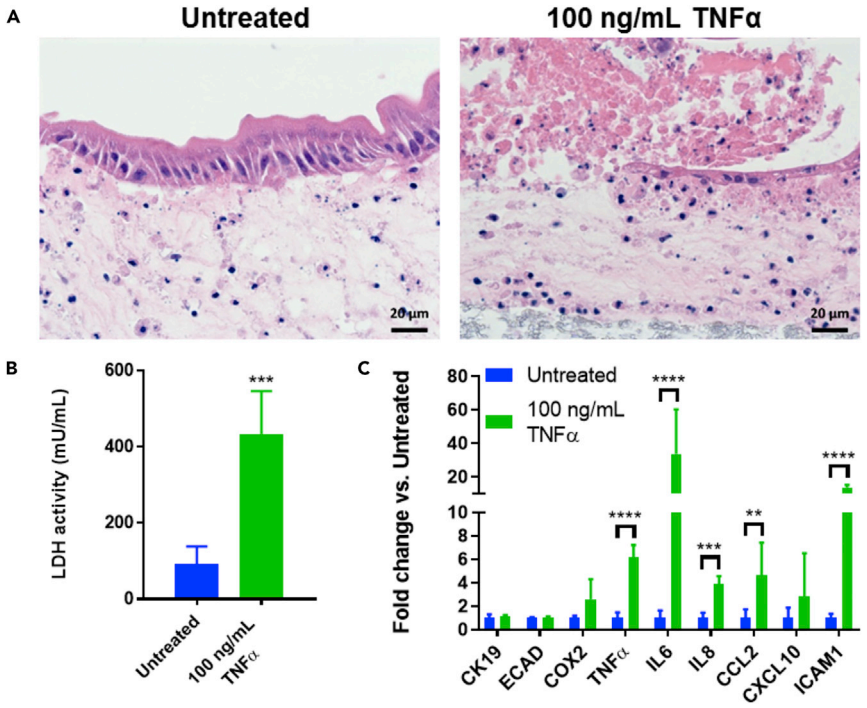

Figure 7. TNF-α-Induced Toxicity in 3D Intestinal Tissue

(A) Tissues treated with TNF-α for 24 hr showed increased epithelial disorganization compared with controls.

(B) Increased LDH activity correlated with changes in cell morphology following TNF-α treatment (n = 5–6).

(C) A subset of genes related to inflammation, *TNF-α*, *IL-6*, *IL-8*, *CCL2*, and *ICAM*, were upregulated in response to TNF-α treatment (n = 3). Level of significance: ***p < 0.001 by t test in (B); **p < 0.01, ***p < 0.001, and ****p < 0.0001 by two-way ANOVA in (C). Data in (B) and (C) are expressed as mean ± SD.

through both inhibition and induction—CYP3A4 activity and PXR-regulated genes were induced in response to rifampicin. The 3D intestinal model demonstrated reproducible midazolam metabolism in tissues separately fabricated from three different donors with interindividual donor variation as expected (Paine et al., 1997). Values were similar to those shown for intestinal slices (van de Kerkhof et al., 2006) and much higher than those reported for 2D systems (Takenaka et al., 2014; Yamaura et al., 2016), suggesting suitability of this model for drug-induced metabolic and transporter studies, which cannot be achieved by previous primary or Caco-2 models (Takenaka et al., 2014; Yamaura et al., 2016).

A differentiating factor of this 3D model over other 3D primary cell systems including organoids and more recent cell-seeded tubular scaffolds (Chen et al., 2017) is the laminar architecture that provides both apical and basal access and compatibility with standard barrier function and directional transport assays. Physiological barrier function was successfully demonstrated by TEER (74.4 ± 24.5 Ω*cm^2) in 3D intestinal tissues at day 10 and maintained through day 21 of culture. Furthermore, tissues could successfully differentiate between low-, intermediate-, and high-permeability substrates such as paracellular marker lucifer yellow and transcellular marker propranolol. With the advantage of physiological TEER values, models with hIECs may yield a better correlation with *in vivo* permeability compared with Caco-2 monolayers with artificially high measurements (840 ± 55 Ω*cm2), which may be due in part to observed differences in E-cadherin expression (Srinivasan et al., 2015). Barrier measurements in the 3D intestinal model were consistent with reported monolayer cultures of adult intestinal epithelial cells (70–120 Ω*cm^2) (Takenaka et al., 2016). These monolayer models, however, are typically limited to <11 days in culture, can suffer from low CYP expression similar to Caco-2 cells, and have not yet been assessed for toxicity or inflammatory response (Kauffman et al., 2013; Takenaka et al., 2014, 2016).

Intestinal efflux and influx transporters are key mediators of absorption for low-permeability drugs. Clinically relevant P-gp and BCRP efflux transporters, which can significantly affect the net fraction of compound absorbed (Bentz et al., 2013; Peters et al., 2016), were correctly expressed in the apical epithelium and

functional in response to known substrates digoxin and topotecan, respectively. The level of efflux in the 3D intestinal tissue model was more similar to that previously observed in 2D human intestinal cell monolayers than with Caco-2 monolayers (Kauffman et al., 2013; Li et al., 2008; Takenaka et al., 2014). Expression of functional transporters suggests that this system could be applied to assess the relative contributions of efflux transporters to drug disposition, or could be used as a potential model for increased absorption by targeting uptake transporters such as PEPT1 and OATP2B1. The dual presence of transporters and enzymes in the 3D intestinal tissue model suggests that it could be used to shed light on complex drug-drug interactions, such as those seen with overlapping P-gp/CYP3A4 substrates (Kim et al., 1999). Furthermore, high expression of enzymes involved in fatty acid metabolism in the 3D intestinal tissue indicates a potential application for evaluating compounds targeting these enzymes to combat obesity (Shi and Cheng, 2009).

GI toxicity is a common clinical adverse event that cannot be accurately predicted or characterized with current *in vitro* or *in vivo* models (Aprile et al., 2015; Boelsterli et al., 2013; Peyrin-Biroulet, 2010). The NSAID indomethacin demonstrated a toxicity response in 3D intestinal tissue with a dose-dependent decrease in barrier function by TEER and corresponding epithelial cell disruption, correlating with previously reported *in vitro* (Tang et al., 1993; Tomisato et al., 2001) and *in vivo* outcomes (Boelsterli et al., 2013). The 3D intestinal tissue also responded to the toxic inflammatory stimulus TNF-α, resulting in epithelial cell death and upregulation of inflammatory genes, consistent with human data (Christophi et al., 2012) and previous Caco-2 studies (Cui et al., 2010; Treede et al., 2009). These data combined with long-term viability suggest that the 3D intestinal model may be applied to characterize other known classes of compounds that have off-target toxicity in the intestine, such as chemotherapeutics (Aprile et al., 2015), to evaluate inflammatory pathways, and to model chronic diseases, such as inflammatory bowel disease (IBD), Crohn disease, and colitis (Aprile et al., 2015; Boelsterli et al., 2013; Peyrin-Biroulet, 2010). Future applications could increase complexity by incorporating additional cell types such as immune cells or cancer cells, and by utilizing healthy and diseased donor material (Fatehullah et al., 2016; VanDussen et al., 2015), to better understand the contribution of each cell type to the disease phenotype and to better characterize candidate modulators for therapeutic intervention on disease-relevant backgrounds.

In conclusion, we provide evidence for a fully human 3D intestinal tissue model composed of primary cells with increased complexity and function compared with standard *in vitro* models. The 3D tissue recapitulates major intestinal features and physiological functions and is designed to provide a flexible platform compatible with barrier function, permeability, metabolism, transport, and toxicity studies.

METHODS

All methods can be found in the accompanying Transparent Methods supplemental file.

SUPPLEMENTAL INFORMATION

Supplemental Information includes Transparent Methods, five figures, and three tables and can be found with this article online at https://doi.org/10.1016/j.isci.2018.03.015.

ACKNOWLEDGMENTS

This work was funded by Organovo and Merck.

AUTHOR CONTRIBUTIONS

Conceptualization, L.R.M., T.V.N., A.P., R.V., E. M.P., S.C.P., D.G.N., K.N.R.; methodology, L.R.M, S.G.-M., V.S., D.G.N., K.N.R.; formal analysis, L.R.M., S.G.-M., V.S., A.V.L., K.N.R.; investigation, L.R.M., S.G.-M., V.S., A.V.L.; Resources, S.C.P.; writing: original draft, L.R.M., K.N.R.; writing: review and editing, L.R.M., T.V.N., V.S., A.P., R.V., E.M.P., S.C.P., D.G.N., K.N.R.; visualization, L.R.M., S.G.-M., A.V.L.; supervision, L.R.M., S.C.P., D.G.N., K.N.R.; project administration, L.R.M., T.V.N., A.P., R.V., E.M.P., S.C.P., D.G.N., K.N.R.; funding acquisition, T.V.N., A.P., R.V., E.M.P., S.C.P., D.G.N., K.N.R.

DECLARATION OF INTERESTS

L.R.M., S.G.-M., V.S., A.V.L., S.C.P., D.G.N., and K.N.R. are currently or have been employed by and may be shareholders of Organovo, Inc. T.V.N., A.P., R.V., and E.M.P. are currently or have been employed by and may be shareholders of Merck.

D.G.N. is also affiliated with Cellular Approaches; T.V.N. is also affiliated with Thermo Fisher Scientific; R.V. is also affiliated with Celgene Corporation; and E.M.P. is also affiliated with Synergy Partners R&D Solutions.

S.C.P. is the Chief Scientific Officer of Organovo, Inc., and is a member of its Executive Committee.

K.N.R., D.G.N., L.R.M., and Organovo, Inc., have a patent related to this work: PCT/US17/61016, ENGINEERED INTESTINAL TISSUE AND USES THEREOF, 10-NOV-2017.

Received: December 13, 2017
Revised: February 28, 2018
Accepted: March 8, 2018
Published: April 27, 2018

REFERENCES

Allen, J.D., van Loevezijn, A., Lakhai, J.M., van der Valk, M., van Tellingen, O., Reid, G., Schellens, J.H., Koomen, G.J., and Schinkel, A.H. (2002). Potent and specific inhibition of the breast cancer resistance protein multidrug transporter in vitro and in mouse intestine by a novel analogue of fumitremorgin C. Mol. Cancer Ther. *1*, 417–425.

Alqahtani, S., Mohamed, L.A., and Kaddoumi, A. (2013). Experimental models for predicting drug absorption and metabolism. Expert Opin. Drug Metab. Toxicol. *9*, 1241–1254.

Aprile, G., Rihawi, K., De Carlo, E., and Sonis, S.T. (2015). Treatment-related gastrointestinal toxicities and advanced colorectal or pancreatic cancer: a critical update. World J. Gastroenterol. *21*, 11793–11803.

Bentz, J., O'Connor, M.P., Bednarczyk, D., Coleman, J.A., Lee, C., Palm, J., Pak, Y.A., Perloff, E.S., Reyner, E., Balimane, P., et al. (2013). Variability in p-glycoprotein inhibitory potency (ic(50)) using various in vitro experimental systems: implications for universal digoxin drug-drug interaction risk assessment decision criteria. Drug Metab. Dispos. *41*, 1347–1366.

Bhatia, S.N., and Ingber, D.E. (2014). Microfluidic organs-on-chips. Nat. Biotechnol. *32*, 760–772.

Boelsterli, U.A., Redinbo, M.R., and Saitta, K.S. (2013). Multiple NSAID-induced hits injure the small intestine: underlying mechanisms and novel strategies. Toxicol. Sci. *131*, 654–667.

Chen, Y., Zhou, W., Roh, T., Estes, M.K., and Kaplan, D.L. (2017). In vitro enteroid-derived three-dimensional tissue model of human small intestinal epithelium with innate immune responses. PLoS One *12*, e0187880.

Chi, C.W., Ahmed, A.R., Dereli-Korkut, Z., and Wang, S. (2016). Microfluidic cell chips for high-throughput drug screening. Bioanalysis *8*, 921–937.

Christophi, G.P., Rong, R., Holtzapple, P.G., Massa, P.T., and Landas, S.K. (2012). Immune markers and differential signaling networks in ulcerative colitis and Crohn's disease. Inflamm. Bowel Dis. *18*, 2342–2356.

Cui, W., Li, L.X., Sun, C.M., Wen, Y., Zhou, Y., Dong, Y.L., and Liu, P. (2010). Tumor necrosis factor alpha increases epithelial barrier permeability by disrupting tight junctions in Caco-2 cells. Braz. J. Med. Biol. Res. *43*, 330–337.

Dantzig, A.H., Shepard, R.L., Cao, J., Law, K.L., Ehlhardt, W.J., Baughman, T.M., Bumol, T.F., and Starling, J.J. (1996). Reversal of P-glycoprotein-mediated multidrug resistance by a potent cyclopropyldibenzosuberane modulator, LY335979. Cancer Res. *56*, 4171–4179.

Fatehullah, A., Tan, S.H., and Barker, N. (2016). Organoids as an in vitro model of human development and disease. Nat. Cell Biol *18*, 246–254.

Jones, C.R., Hatley, O.J., Ungell, A.L., Hilgendorf, C., Peters, S.A., and Rostami-Hodjegan, A. (2016). Gut wall metabolism. Application of pre-clinical models for the prediction of human drug absorption and first-pass elimination. AAPS J. *18*, 589–604.

Kauffman, A.L., Gyurdieva, A.V., Mabus, J.R., Ferguson, C., Yan, Z., and Hornby, P.J. (2013). Alternative functional in vitro models of human intestinal epithelia. Front Pharmacol. *4*, 79.

Kim, H.J., Huh, D., Hamilton, G., and Ingber, D.E. (2012). Human gut-on-a-chip inhabited by microbial flora that experiences intestinal peristalsis-like motions and flow. Lab Chip *12*, 2165–2174.

Kim, R.B., Wandel, C., Leake, B., Cvetkovic, M., Fromm, M.F., Dempsey, P.J., Roden, M.M., Belas, F., Chaudhary, A.K., Roden, D.M., et al. (1999). Interrelationship between substrates and inhibitors of human CYP3A and P-glycoprotein. Pharm. Res. *16*, 408–414.

King, S.M., Higgins, J.W., Nino, C.R., Smith, T.R., Paffenroth, E.H., Fairbairn, C.E., Docuyanan, A., Shah, V.D., Chen, A.E., Presnell, S.C., et al. (2017). 3D proximal tubule tissues recapitulate key aspects of renal physiology to enable nephrotoxicity testing. Front. Physiol. *8*, 123.

Li, H., Jin, H.E., Kim, W., Han, Y.H., Kim, D.D., Chung, S.J., and Shim, C.K. (2008). Involvement of P-glycoprotein, multidrug resistance protein 2 and breast cancer resistance protein in the transport of belotecan and topotecan in Caco-2 and MDCKII cells. Pharm. Res. *25*, 2601–2612.

Li, M., de Graaf, I.A., and Groothuis, G.M. (2016). Precision-cut intestinal slices: alternative model for drug transport, metabolism, and toxicology research. Expert Opin. Drug Metab. Toxicol. *12*, 175–190.

Musther, H., Olivares-Morales, A., Hatley, O.J., Liu, B., and Rostami Hodjegan, A. (2014). Animal versus human oral drug bioavailability: do they correlate? Eur. J. Pharm. Sci. *57*, 280–291.

Neurath, M.F. (2014). New targets for mucosal healing and therapy in inflammatory bowel diseases. Mucosal Immunol. *7*, 6–19.

Nguyen, D.G., Funk, J., Robbins, J.B., Crogan-Grundy, C., Presnell, S.C., Singer, T., and Roth, A.B. (2016). Bioprinted 3D primary liver tissues allow assessment of organ-level response to clinical drug induced toxicity in vitro. PLoS One *11*, e0158674.

Paine, M.F., Khalighi, M., Fisher, J.M., Shen, D.D., Kunze, K.L., Marsh, C.L., Perkins, J.D., and Thummel, K.E. (1997). Characterization of interintestinal and intraintestinal variations in human CYP3A-dependent metabolism. J. Pharmacol. Exp. Ther. *283*, 1552–1562.

Peters, S.A., Jones, C.R., Ungell, A.L., and Hatley, O.J.D. (2016). Predicting drug extraction in the human gut wall: assessing contributions from drug metabolizing enzymes and transporter proteins using preclinical models. Clin. Pharmacokinet. *55*, 673–696.

Peyrin-Biroulet, L. (2010). Anti-TNF therapy in inflammatory bowel diseases: a huge review. Minerva Gastroenterol. Dietol. *56*, 233–243.

Prueksaritanont, T., Gorham, L.M., Hochman, J.H., Tran, L.O., and Vyas, K.P. (1996). Comparative studies of drug-metabolizing enzymes in dog, monkey, and human small intestines, and in Caco-2 cells. Drug Metab. Dispos. *24*, 634–642.

Sato, T., Stange, D.E., Ferrante, M., Vries, R.G., Van Es, J.H., Van den Brink, S., Van Houdt, W.J., Pronk, A., Van Gorp, J., Siersema, P.D., et al. (2011). Long-term expansion of epithelial organoids from human colon, adenoma, adenocarcinoma, and Barrett's epithelium. Gastroenterology *141*, 1762–1772.

Schweinlin, M., Wilhelm, S., Schwedhelm, I., Hansmann, J., Rietscher, R., Jurowich, C., Walles, H., and Metzger, M. (2016). Development of an

advanced primary human in vitro model of the small intestine. Tissue Eng. Part C Methods *22*, 873–883.

Shi, Y., and Cheng, D. (2009). Beyond triglyceride synthesis: the dynamic functional roles of MGAT and DGAT enzymes in energy metabolism. Am. J. Physiol. Endocrinol. Metab. *297*, E10–E18.

Sinagoga, K.L., and Wells, J.M. (2015). Generating human intestinal tissues from pluripotent stem cells to study development and disease. EMBO J. *34*, 1149–1163.

Spence, J.R., Mayhew, C.N., Rankin, S.A., Kuhar, M., Vallance, J.E., Tolle, K., Hoskins, E.E., Kalinichenko, V.V., Wells, S.I., Zorn, A.M., et al. (2011). Directed differentiation of human pluripotent stem cells into intestinal tissue in vitro. Nature *470*, 105–109.

Srinivasan, B., Kolli, A.R., Esch, M.B., Abaci, H.E., Shuler, M.L., and Hickman, J.J. (2015). TEER measurement techniques for in vitro barrier model systems. J. Lab. Autom. *20*, 107–126.

Takenaka, T., Harada, N., Kuze, J., Chiba, M., Iwao, T., and Matsunaga, T. (2014). Human small intestinal epithelial cells differentiated from adult intestinal stem cells as a novel system for predicting oral drug absorption in humans. Drug Metab. Dispos. *42*, 1947–1954.

Takenaka, T., Harada, N., Kuze, J., Chiba, M., Iwao, T., and Matsunaga, T. (2016). Application of a human intestinal epithelial cell monolayer to the prediction of oral drug absorption in humans as a superior alternative to the Caco-2 cell monolayer. J. Pharm. Sci. *105*, 915–924.

Tang, A.S., Chikhale, P.J., Shah, P.K., and Borchardt, R.T. (1993). Utilization of a human intestinal epithelial cell culture system (Caco-2) for evaluating cytoprotective agents. Pharm. Res. *10*, 1620–1626.

Tomisato, W., Tsutsumi, S., Rokutan, K., Tsuchiya, T., and Mizushima, T. (2001). NSAIDs induce both necrosis and apoptosis in Guinea pig gastric mucosal cells in primary culture. Am. J. Physiol. Gastrointest. Liver Physiol. *281*, G1092–G1100.

Treede, I., Braun, A., Jeliaskova, P., Giese, T., Fullekrug, J., Griffiths, G., Stremmel, W., and Ehehalt, R. (2009). TNF-alpha-induced up-regulation of pro-inflammatory cytokines is reduced by phosphatidylcholine in intestinal epithelial cells. BMC Gastroenterol. *9*, 53.

van de Kerkhof, E.G., Ungell, A.L., Sjoberg, A.K., de Jager, M.H., Hilgendorf, C., de Graaf, I.A., and Groothuis, G.M. (2006). Innovative methods to study human intestinal drug metabolism in vitro: precision-cut slices compared with ussing chamber preparations. Drug Metab. Dispos. *34*, 1893–1902.

VanDussen, K.L., Marinshaw, J.M., Shaikh, N., Miyoshi, H., Moon, C., Tarr, P.I., Ciorba, M.A., and Stappenbeck, T.S. (2015). Development of an enhanced human gastrointestinal epithelial culture system to facilitate patient-based assays. Gut *64*, 911–920.

Wang, X., Yamamoto, Y., Wilson, L.H., Zhang, T., Howitt, B.E., Farrow, M.A., Kern, F., Ning, G., Hong, Y., Khor, C.C., et al. (2015). Cloning and variation of ground state intestinal stem cells. Nature *522*, 173–178.

Watson, C.L., Mahe, M.M., Munera, J., Howell, J.C., Sundaram, N., Poling, H.M., Schweitzer, J.I., Vallance, J.E., Mayhew, C.N., Sun, Y., et al. (2014). An in vivo model of human small intestine using pluripotent stem cells. Nat. Med. *20*, 1310–1314.

Yamaura, Y., Chapron, B.D., Wang, Z., Himmelfarb, J., and Thummel, K.E. (2016). Functional comparison of human colonic carcinoma cell lines and primary small intestinal epithelial cells for investigations of intestinal drug permeability and first-pass metabolism. Drug Metab. Dispos. *44*, 329–335.

Yin, X., Farin, H.F., van Es, J.H., Clevers, H., Langer, R., and Karp, J.M. (2014). Niche-independent high-purity cultures of Lgr5+ intestinal stem cells and their progeny. Nat. Methods *11*, 106–112.

ISCI, Volume *2*

Supplemental Information

Bioprinted 3D Primary Human Intestinal Tissues Model Aspects of Native Physiology and ADME/Tox Functions

Lauran R. Madden, Theresa V. Nguyen, Salvador Garcia-Mojica, Vishal Shah, Alex V. Le, Andrea Peier, Richard Visconti, Eric M. Parker, Sharon C. Presnell, Deborah G. Nguyen, and Kelsey N. Retting

Supplemental Figures

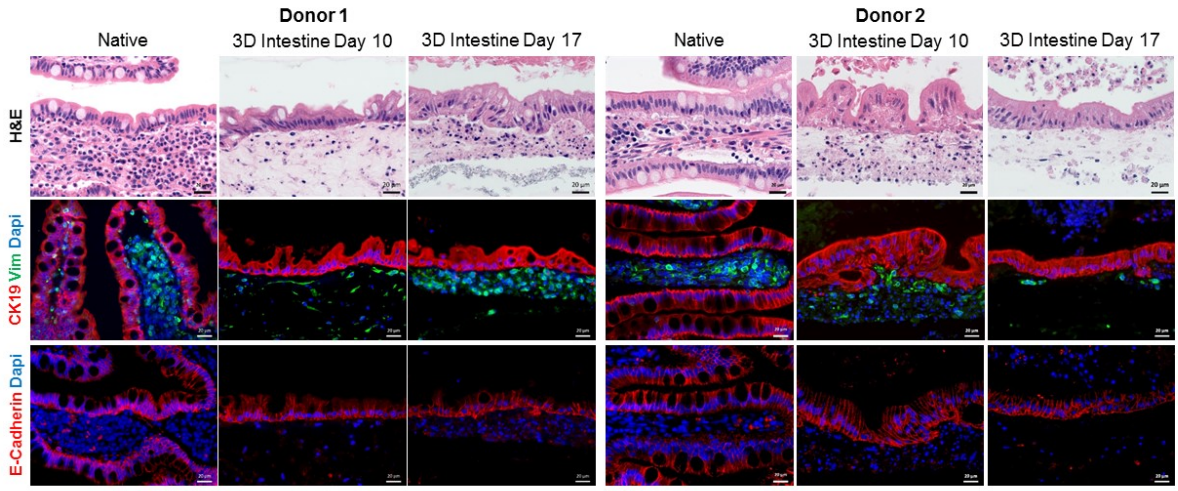

Figure S1, related to Figure 1. Comparative histology of native intestine and two donors of 3D intestinal tissue. H&E shows that both native intestine and 3D intestine have a bi-layered structure containing CK19 expressing epithelial cells and vimentin stained myofibroblasts. Native intestine and both donors of 3D intestinal tissue express E-Cadherin continuously within the epithelium, indicating tight junction formation.

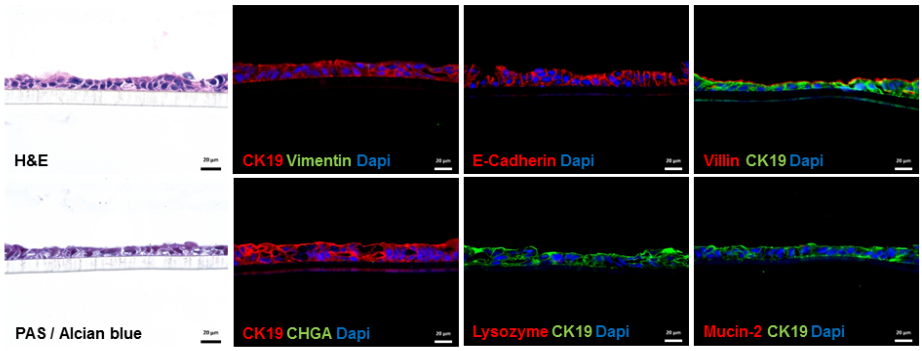

Figure S2, related to Figure 1. Caco-2 histology. Day 21 monolayers of Caco-2 cells were stained for general and specialized cell subtype epithelial markers. Caco-2 express CK19, E-Cadherin, and villin across the monolayer. No staining was observed for chromogranin, lysozyme, or mucin-2.

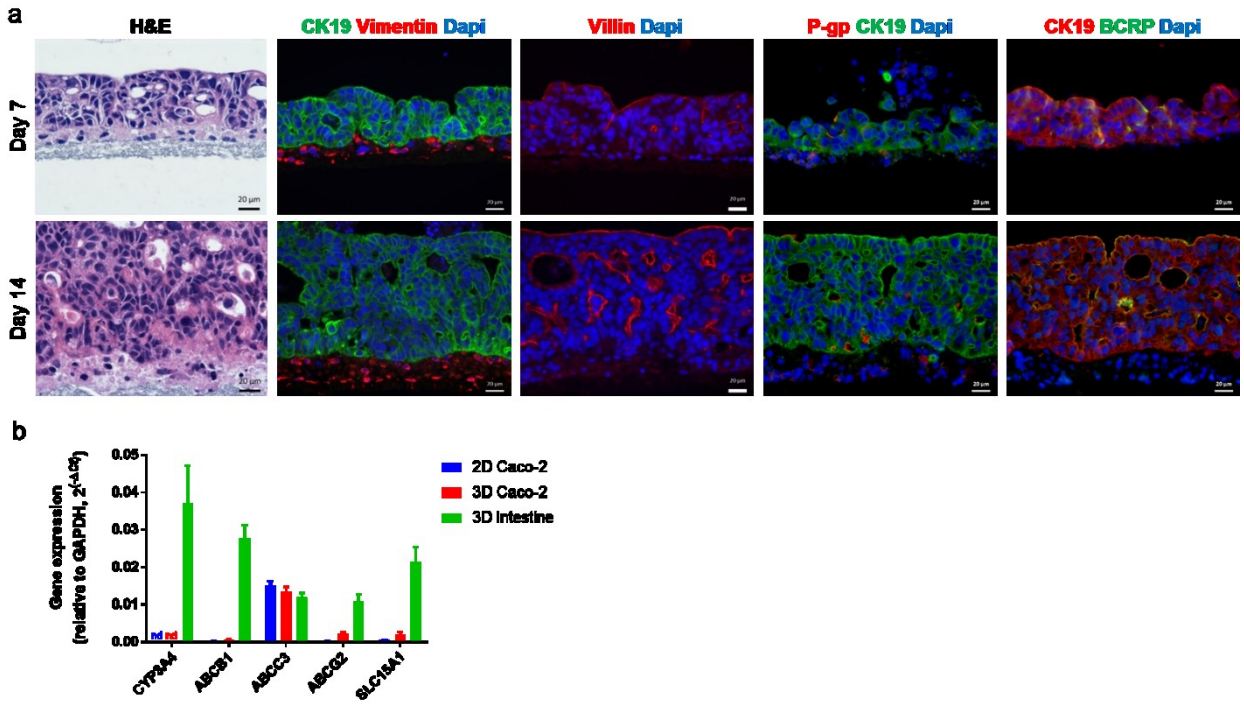

Figure S3, related to Figure 1 and Figure 5. 3D Bioprinted Caco-2 tissues form a thick bi-layered structure. CK19 expressing Caco-2 cells expand over time while vimentin positive IMF remain constant (a). Villin staining shows disorientation of epithelial cells and the formation of cyst-like structures over time. Low amounts of P-gp are present at both days 7 and 14. While BCRP expression increased over time, much is found in the cyst-like structures compared to normal apical expression. (b) Gene expression of several key transporters and *CYP3A4* is reduced or absent in 2D and 3D Caco-2 tissues compared to 3D intestinal tissue fabricated with primary human intestinal epithelial cells (n=3). nd= not determined. Data are represented as ± STD.

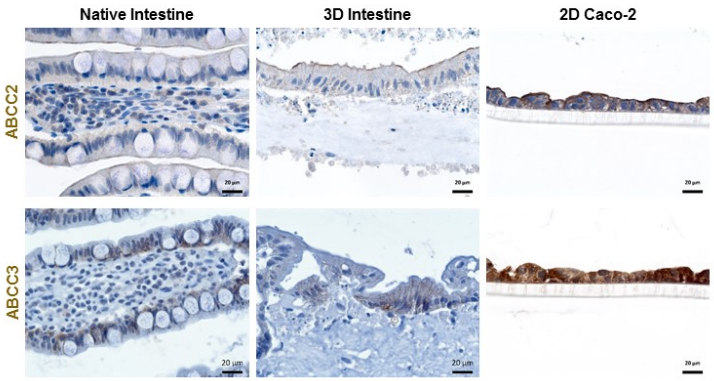

Figure S4, related to Figure 5. MRP2 and MRP3 transporter expression. Native intestine, 3D intestinal tissue, and Caco-2 monolayers were compared for expression of MRP2 (ABCC2) and MRP3 (ABCC3). Similar levels of MRP staining were observed between native intestine and 3D intestine with higher levels seen in Caco-2 monolayers.

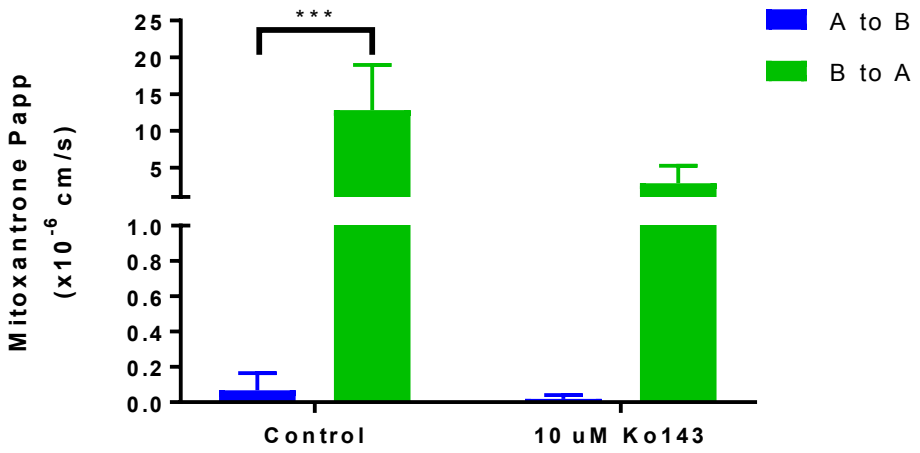

Figure S5, related to Figure 5. BCRP efflux of mitoxantrone. Low permeability A to B of mitoxantrone, a BCRP substrate, was observed with much higher permeability in the B to A direction, efflux ratio = 190. In the presence of BCRP inhibitor Ko143, Mitoxantrone permeability B to A decreased and efflux ratio reduced to 145. Note: samples for A to B were near or below limit of detection. (n=4) Level of significance: ***P < 0.001 by two-way ANOVA. Data are represented as ± STD.

Supplemental Tables

Table S1, related to Figure 3. Interindividual variability in midazolam metabolism of 3D intestine. Data are represented as ± STD.

	Untreated	Ketoconazole		Rifampicin	
	pmol/min/mg	pmol/min/mg	% untreated	pmol/min/mg	% untreated
Donor 1	19.3 ± 1.9	2.7 ± 0.2	13.9 ± 1.0	26.2 ± 3.9	136 ± 20
Donor 2	2.85 ± 0.59	0.81 ± 0.2	28.4 ± 7.5	10.1 ± 2.0	355 ± 69
Donor 3	3.6 ± 3.6	0.67 ± 0.1	18.6 ± 3.4	10.1 ± 0.9	281 ± 25

Table S2, related to Figure 4. Comparison of human absorbed fraction (Fa) to P_{app} ($x10^{-6}$ cm/s) of 3D intestine and 2D monolayers. Lucifer yellow (n=28), mitoxantrone (n=4), topotecan (n=4), digoxin (n=6), propranolol (n=5). Data are represented as ± STD for 3D intestine.

Compound	Fa (%)	P_{app} ($x10^6$ cm/s)			Pathway	Ref. for 2D hIEC and Caco-2 values
		3D intestine	2D hIEC	2D Caco-2		
Lucifer yellow	n/a	0.45 ± 1.5	< 1	< 1	Paracellular	Bentz et al. (2013) and Kauffman et al. (2013)
Mitoxantrone	n/a	0.2 ± 0.03	~0.2	~0.1	Transcellular / BCRP, P-gp	Takenaka et al. (2014)
Topotecan	30	3.1 ± 0.63	0.78 ± 0.14	0.35 ± 0.06; 3.67 ± 0.02	Transcellular / BCRP, P-gp	Takenaka et al. (2014) Li et al. (2008)
Digoxin	75	8.53 ± 2.02	3.5 ± 0.2 ~6	0.96 ± 0.03	Transcellular / P-gp	Takenaka et al. (2014) and Takenaka et al. (2016)
Propranolol	93	14.8 ± 1.96	22 ± 2	41 ± 3	Transcellular	Takenaka et al. (2016)

Table S3, related to Figure 5. Comparison of compound transport in 3D intestine and 2D monolayers.

Compound	Efflux Ratio ((B→A)/(A→B))			Pathway	Ref. for 2D hIEC and Caco-2 values
	3D intestine	2D hIEC	2D Caco-2		
Digoxin	2.1	2.2; 4-8	3.1; 6.1 - 102	Transcellulary / P-gp	Takenaka et al. (2014); Kauffman et al. (2013); Benzt et al. (2013)
Topotecan	8.8	n/a	>2	Transcellular / BCRP, P-gp	Li et al (2008)
Mitoxantrone	190	38.2	4	Transcellular / BCRP, P-gp	Takenaka et al. (2014)

Transparent Methods

Materials used in experimental procedures

REAGENT or RESOURCE	SOURCE	IDENTIFIER
Antibodies		
Anti-cytokeratin 19 antibody [EP1580Y]	Abcam	ab52625; RRID AB_2281020
Anti-cytokeratin 19 antibody [A53-B/A2]	Abcam	ab7754; RRID AB_306048
Vimentin antibody (V9)	SCBT	sc-6260; RRID AB_628437
Chr-A antibody (C-20)	SCBT	sc-1488; RRID AB_2276319
Anti-E-Cadherin antibody [EP700Y]	Abcam	ab40772; RRID AB_731493
Anti-Villin antibody [SP145]	Abcam	ab130751; RRID AB_11159755
Mucin 2 Antibody (H-300)	SCBT	sc-15334; RRID AB_2146667
Anti-Lysozyme antibody [EPR2994(2)]	Abcam	ab108508; RRID AB_10861277
Anti-P Glycoprotein antibody [EPR10364-57]	Abcam	ab170904; RRID AB_2687930
Anti-BCRP/ABCG2 antibody [BXP-21]	Abcam	ab3380; RRID AB_303758
Anti—MRP2 antibody [M2 III-6]	Abcam	ab3373: RRID AB_303751
Anti-MRP3 antibody [M3II-9]	Abcam	ab3375; RRID AB_303753
Oligonucleotides		
18s rRNA	Applied Biosystems	Assay ID: Hs99999901_s1
ABCB1	Applied Biosystems	Assay ID: Hs00184500_m1
ABCC2	Applied Biosystems	Assay ID: Hs00166123_m1
ABCC3	Applied Biosystems	Assay ID: Hs00978473_m1
ABCG2	Applied Biosystems	Assay ID: Hs01053790_m1
CCL2	Applied Biosystems	Assay ID: Hs00234140_m1
CDH1	Applied Biosystems	Assay ID: Hs01023894_m1
CDH17	Applied Biosystems	Assay ID: Hs00900408_m1
CDX2	Applied Biosystems	Assay ID: Hs01078080_m1
CES2	Applied Biosystems	Assay ID: Hs01077945_m1
CHGA	Applied Biosystems	Assay ID: Hs00900375_m1

CK19	Applied Biosystems	Assay ID: Hs00761767_s1
CXCL8	Applied Biosystems	Assay ID: Hs00174103_m1
CXCL10	Applied Biosystems	Assay ID: Hs00171042_m1
CYP2C19	Applied Biosystems	Assay ID: Hs00426380_m1
CYP2C8	Applied Biosystems	Assay ID: Hs02383390_s1
CYP2C9	Applied Biosystems	Assay ID: Hs02383631_s1
CYP2D6	Applied Biosystems	Assay ID: Hs02576167_m1
CYP2J2	Applied Biosystems	Assay ID: Hs00356035_m1
CYP2S1	Applied Biosystems	Assay ID: Hs00258076_m1
CYP3A4	Applied Biosystems	Assay ID: Hs00604506_m1
CYP3A5	Applied Biosystems	Assay ID: Hs00241417_m1
DGAT1	Applied Biosystems	Assay ID: Hs01017541_m1
GAPDH	Applied Biosystems	Assay ID: 4326317E
GSTP1	Applied Biosystems	Assay ID: Hs00943350_g1
ICAM1	Applied Biosystems	Assay ID: Hs00164932_m1
IL-6	Applied Biosystems	Assay ID: Hs00174131_m1
IL-8	Applied Biosystems	Assay ID: Hs00991010_m1
LGR5	Applied Biosystems	Assay ID: Hs00969422_m1
LYZ	Applied Biosystems	Assay ID: Hs00426232_m1
MOGAT2	Applied Biosystems	Assay ID: Hs00228268_m1
MTTP	Applied Biosystems	Assay ID: Hs00165177_m1
MUC2	Applied Biosystems	Assay ID: Hs03005103_g1
NR1I2	Applied Biosystems	Assay ID: Hs01114267_m1
NR1I3	Applied Biosystems	Assay ID: Hs00901571_m1
COX-2	Applied Biosystems	Assay ID: Hs00153133_m1
SLC10A2	Applied Biosystems	Assay ID: Hs01001557_m1
SLC15A1	Applied Biosystems	Assay ID: Hs00192639_m1

SLC16A1	Applied Biosystems	Assay ID: Hs01560299_m1
SLC28A1	Applied Biosystems	Assay ID: Hs00984403_m1
SLC51A	Applied Biosystems	Assay ID: Hs00380895_m1
SLC51B	Applied Biosystems	Assay ID: Hs01057182_m1
SLC7A5	Applied Biosystems	Assay ID: Hs01001183_m1
SLC7A8	Applied Biosystems	Assay ID: Hs00794796_m1
SLCO2B1	Applied Biosystems	Assay ID: Hs01030343_m1
TNF	Applied Biosystems	Assay ID: Hs01113624_g1
UGT1A1	Applied Biosystems	Assay ID: Hs02511055_s1
VDR	Applied Biosystems	Assay ID: Hs00172113_m1
VIL1	Applied Biosystems	Assay ID: Hs01031724_m1
Chemicals, Peptides, and Recombinant Proteins		
Digoxin	Sigma Aldrich	Cat # 04599-50MG
Zosuquidar	Sigma Aldrich	Cat # SML1044-5MG
Lucifer yellow	Sigma Aldrich	Cat # L0144
Mitoxantrone	Cayman chemicals	Cat # 14842
Topotecan	Cayman chemicals	Cat # 14129
Ko143	Cayman chemicals	Cat # 15215
Propranolol	Cayman chemicals	Cat # 17291
Ketoconazole	Sigma Aldrich	Cat # K1003-100MG
Sulfaphenazole	Cayman chemicals	Cat # 14844
Rifampicin	Sigma Aldrich	Cat # R8883-150MG
Midazolam	Cayman chemicals	Cat # 19391
Indomethacin	Cayman chemicals	Cat # 70270
TNF α	R&D Systems	Cat # 210-TA-005/CF
Critical Commercial Assays		
RNeasy Mini Kit	Qiagen	Cat # 74106
SuperScript III First-Strand Synthesis SuperMix for qRT-PCR	ThermoFisher	Cat # 11752050
TaqMan Universal Master Mix II with UNG	ThermoFisher	Cat # 4440038
TaqMan Fast Virus 1-Step Master mix	ThermoFisher	Cat # 4444434
P450-Glo CYP2C9 Assay	Promega	Cat # V8791
P450-Glo CYP3A4 Assay – Luciferin IPA	Promega	Cat # V9001
Pierce BCA Protein Assay kit	Thermo Fisher Scientific	Cat # 23227
Lactate dehydrogenase assay kit	Abcam	Cat # 102526
Prostaglandin E2 ELISA	Cayman chemicals	Item # 514010

Experimental Models: Cell Lines		
Caco-2 cell line	Sigma	Cat # 86010202-1VL; RRID CVCL_0025
Human intestinal myofibroblasts (IMF)	Lonza	
Other		
NovoGen Bioprinter	Organovo	n/a
EVOM2 Epithelial Voltohmmeter	World Precision Instruments	Item # EVOM2
STX2 chopstick electrodes	World Precision Instruments	Item # STX2

Intestinal cell isolation and cell culture

We acknowledge the use of tissues procured by the National Disease Research Interchange (NDRI) with support from NIH grant 2 U42 OD011158 and protocol approved by NDRI and Organovo Inc. Native intestine was processed from five donors, three of which resulted in primary intestinal epithelial cell isolation (1: 18 / M; 2(native donor A): 29 / M; 3: 23 / M; 4(native donor B): 36 / M; 5(native donor C): 57 / M). Adult human intestinal myofibroblast (IMF) cells were sourced from Lonza (age/sex not available). The Caco-2 cell line (derived from a primary colonic tumor of a 72 year old male) was used at passage 46 as a comparison to primary human cells.

Human intestinal epithelial cells (hIEC) were isolated from and cultured according to reported methods (Sato et al., 2011, Lahar et al., 2011). Briefly, ileal tissue was received on ice, aseptically cleaned with ice cold PBS, then cut into three inch segments. Segments were opened and mucosectomy was performed, then tissues were minced to about five by five millimeter chunks. Tissue pieces were washed vigorously in PBS by vortexing, then epithelial cells were dissociated by incubation in PBS with EDTA and DTT. Cells were dissociated from the tissue by repeat vortexing with PBS changes between each vortex. Epithelial cells were plated in growth factor reduced Matrigel with intestinal growth media comprised of Advanced DMEM/F12 with supplements. Adult human intestinal myofibroblast (IMF) cells and Caco-2 cells were cultured according to manufacturer's instructions.

3D bioprinting and tissue culture

3D intestinal tissues comprised of an interstitium and epithelium were manufactured by Organovo (San Diego, CA) using a proprietary bioprinting platform and standard protocols previously described (Nguyen et al., 2016, King et al., 2017). In brief, cultured cells were resuspended in thermo-responsive Novogel® Bio-ink and bioprinted onto membranes of standard 24-well 3 µm Transwell® culture permeable supports using a NovoGen® Bioprinter (Organovo Inc., San Diego, CA) with the interstitial and epithelial compartments comprised of IMF and hIEC, respectively or IMF and Caco-2 cells, respectively. Tissues were then cultured in 3D intestinal media containing Advanced DMEM/F12 with supplements at 37°C. Tissues were maintained in 3D intestinal media (Organovo Inc., San Diego, CA) for up to 21 days with media exchanges every day and were washed apically with PBS every other day. After printing, intestinal tissues were cultured for ten days prior to initiation of studies to allow barrier formation. Caco-2 monolayer studies were conducted according to previously reported studies (Bentz et al., 2013).

Briefly, cells were seeded at 30,000 cells/cm^2 per well onto standard 24-well Transwell® permeable supports and cultured at air-liquid interface in DMEM with L-glutamine + 10% FBS with media changes every 48 hours. Monolayers were grown for 21 days at 37°C then qualified for used by TEER (785 ± 56 $\Omega*cm^2$).

Histology

Tissues were fixed in 2% paraformaldehyde solution (10mM calcium chloride, 50 mM sucrose in PBS) processed, and paraffin embedded by standard techniques. Sections were stained by hematoxylin and eosin (H&E) and Periodic acid-Schiff (PAS) / Alcian blue (pH 2.5) using standard protocols. Immunofluorescent staining using a panel of antibodies (Key resource table) to specific cell types or components was performed following deparaffinization, heat-mediated antigen retrieval, and permeabilization. Signal was detected using the appropriate fluorescently conjugated secondary antibodies. Staining methods and antibodies were validated on normal human small intestine control tissue prior to use on bioprinted tissues.

Gene Expression

RNA was extracted by RNeasy Mini Kit and analyzed by real-time quantitative polymerase chain reaction (RT-PCR; qPCR) using TaqMan gene expression assays (see table). TaqMan Array analysis (Figure 2) was carried out using the ViiA 7 System with 200ng of cDNA, synthesized using SuperScript III First-Strand Synthesis SuperMix for qRT-PCR, per channel quantified with a NanoDrop spectrophotometer. TaqMan Array gene expression was analyzed using ExpressionSuite Software and shown as relative expression ($2^{-(\Delta Ct)}$) calculated using comparative Ct method to endogenous control 18S ($\Delta Ct = Ct_{target} - Ct_{18S}$) and analyzed as a ratio to amount of a gene present compared to epithelial-specific cytokeratin 19 ($\Delta Ct_{CK19} = Ct_{CK19} - Ct_{18S}$): Relative quantity = $(2^{-(\Delta Ct)})/(2^{-(\Delta CtCK19)})$. A heatmap of the TaqMan Array data was generated with Spotfire (TIBCO Software Inc.). The values displayed were calculated by taking the log of the Relative quantity = $(2^{-(\Delta Ct)})/(2^{-(\Delta CtCK19)})$ (calculation methods shown above), the MIN was -4.90 and MAX was 0.49. The samples were clustered by unweighted pair group method (UPGMA) with a correlation distance measurement and average value ordering weight. The gene categories were clustered by UPGMA with a Euclidean distance measurement and average value ordering weight. Individual gene expression data for 3D intestinal tissues and Caco-2 are expressed as an average of three biological replicates and plotted with GraphPad Prism. Quantitative PCR reactions were conducted with TaqMan Universal Master Mix II with UNG, under the following conditions: 50°C for 2 minutes; 95°C for 10 minutes; and 40 cycles of amplification at 95°C for 15 seconds followed by 60°C for 1 minute. Single-tube assays (Figure 3f, 7c, S3b) were carried out using the StepOnePlus System with 20 ng of DNase treated RNA quantified with a NanoDrop spectrophotometer. Fast RT-PCR reactions were conducted with Fast 1-Step mix under the following conditions: reverse transcription at 50°C for 5 minutes; RT inactivation/denaturation at 95°C for 20 seconds; and 45 cycles of amplification at 95°C for 3 seconds followed by 60°C for 30 seconds. Single tube assay gene expression data (Figure 3f, 7c, S3c) was normalized to GAPDH endogenous control and calculated according to the ΔΔCt method. Data is

graphed as a fold change of treated relative to untreated to obtain the effects of treatment induction on gene expression. Gene targets were first normalized to endogenous control GAPDH ($\Delta Ct = Ct_{target} - Ct_{GAPDH}$) and then calculated relative to treatment ($\Delta\Delta Ct = \Delta Ct_{treated} - \Delta Ct_{untreated}$). Final data is represented as $2^{-\Delta\Delta Ct}$ for fold-change and graphed with GrahpPad Prism. Data is expressed as the average of 3-4 grouped biological replicates plus or minus the standard deviation; each biological replicate is represented by the average of 2 technical replicates.

TEER measurements

The EVOM2 Epithelial Voltohmmeter with STX2 chopstick electrodes was used to measure construct transepithelial electrical resistance (TEER). Instrument was calibrated with a 1000 Ω resistor prior to measurements and an empty transwell used as a blank. Constructs were equilibrated to room temperature and switched to basal media for readings. The blank transwell and all samples were measured three times. Samples and blanks were measured in triplicate, then each averaged and used in the following calculations:

$$R_{TISSUE}(\Omega) = R_{TISSUE} - R_{BLANK}$$

$$TEER_{REPORTED} = R_{TISSUE}(\Omega) x M_{AREA}(cm^2)$$

Where $M_{AREA} = 0.33\ cm^2$

Permeability and transport

For permeability assays, compound was prepared at 10-100 µM in Advanced DMEM/F12 media then 100 µL of compound was added to the apical side and 600 µL of blank media was added to the basal side. Linearity of flux was established by assessing Rhodamine 123 transport at 20 minute intervals, however, single time points were used for test compounds as most compounds could not be detected at short time intervals. After 60 minutes (Lucifer yellow and mitoxantrone) or 120 minutes (digoxin, propranolol, topotecan), the basal side was sampled for analysis. Digoxin and propranolol concentrations were determined by mass spectrometry and Lucifer yellow, topotecan, and mitoxantrone concentrations were determined by fluorescence using a BMG POLARstar. For transport assays, tissues were pre-incubated with vehicle or inhibitor for 30 minutes prior to assay. Compounds for transport were assayed from both apical to basal (A to B) and basal to apical (B to A) transport. Efflux ratio was calculated as the ratio of (B to A)/(A to B).

Metabolic activity assays

CYP2C9 and CYP3A4 activities were measured by P450-Glo luminescent assays per manufacturer's instructions. Briefly, tissues were washed with Advanced DMEM/F12 media plus vehicle or inhibitor (ketoconazole for CYP3A4, sulfaphenazole for CYP2C9) for 30 minutes. Tissues were incubated with P450-Glo substrates in the presence of vehicle or inhibitor for one hour then supernatant was transferred to white assay plates and incubated with luminescent detection reagent. Luminescence was

detected using a BMG POLARstar. Tissues were lysed with RIPA buffer and protein quantified using Pierce BCA Protein Assay kit.

CYP3A4 inhibition and induction were assessed by metabolism of midazolam. For induction studies, tissues were pre-incubated with 20 uM rifampicin for 72 hours followed by 30 minutes in either blank vehicle or inhibitor before initiating treatment with midazolam. To test CYP3A4 activity, tissues were incubated with 10 µM midazolam then supernatant was assayed for both parent drug and the 1-OH metabolite by mass spectrometry. Tissues were then lysed with RIPA buffer and protein quantified or lysed for RNA extraction.

Mass spectrometry

Detection of midazolam, digoxin, and propranolol were performed by mass spectrometry. Analyst was used to determine peak areas and generate standard curves for each compound. Sample values were quantified using the standard curve and normalized to the internal reference compound.

Midazolam. Stock solutions of 20 µM of midazolam and 10 µM of α-hydroxy midazolam were prepared in 50/50 methanol:blank media, combined at 1:1 serial dilutions were prepared to generate a standard curve. Each 50 µL standard or sample was diluted with 50 µL of midazolam-d4 (1 µg/mL) prepared in methanol then 10 µL was injected for determination of metabolite formation (1-OH midazolam). Each sample was subsequently diluted with 100 µL of methanol and re-injected for determination of midazolam concentration. LC–MS/MS analyses were performed using an Agilent 1200 HPLC system coupled to a PE Sciex API 4000 Qtrap tandem mass spectrometer with a Turbo Ionspray. The analytical column was an Agilent Zorbax XDB C8, 50 mm × 2.1 mm, 3.5 um and was kept at ambient temperature. Mobile phase A consisted of water with 0.1% formic acid and mobile phase B consisted of acetonitrile with 0.1% formic acid. The total run time was 4 min with an initial gradient of 5% mobile phase B held for 1 minute, followed by an increase to 95% B over 2 minutes. Mobile phase B was held at 95% B for one minute followed by re-equilibration to initial conditions for 2 minutes. The flow rate was set at 0.6 mL/min. The Ionspray needle was maintained at 5.0 kV. The turbo gas temperature was 500 ◦C and the CAD gas flow setting was medium. Curtain gas, GS1 and GS2 were 10, 20, and 0, respectively. The declustering potentials (DP) and the entrance potential (EP) was 81 and 10 V for midazolam, respectively. The mass spectrometer was operated in MRM mode with collision energy (CE) of 39 V and a collision cell exit potential (CXP) of 16. The transitions (precursor to product) monitored were *m/z* 326→291 for midazolam, 342→203 for 1-OH midazolam, and m/z 330→295 for midazolam-d4 (IS) in positive mode. The dwell time was 150 ms for all analytes and the internal standard. Both Q1 and Q3 quadrupoles were maintained at unit resolution.

Digoxin. A stock solution of 10 µM of digoxin was prepared in 50/50 methanol:blank media. Each stock was combined in a ratio of 1:1 and serial dilutions were prepared to generate a standard curve. Twenty-five µL of each standard or sample was mixed with 200 µL of the internal standard, digitoxin (1 µg/mL)

prepared in methanol. 20 µL was injected for determination of digoxin concentration. LC–MS/MS analyses were performed using an Agilent 1200 HPLC system coupled to a PE Sciex API 4000 Qtrap tandem mass spectrometer with a Turbo Ionspray. The analytical column was a Phenomenex Synergi Max RP, 50 mm × 2.1 mm, 4 um and was kept at ambient temperature. Mobile phase A consisted of water with 5 mM ammonium formate (pH 3.4) and mobile phase B consisted of acetonitrile with 0.1% formic acid. The total run time was 5 min with an initial gradient of 5% mobile phase B at a flow rate of 0.750 mL/mL The initial conditions were held for 1 minute, followed by an increase to 99% B and 1 mL/min over 1.5 minutes. Mobile phase B was held at 99% B for one minute followed by re-equilibration to initial conditions for 2 minutes. The Ionspray needle was maintained at 5.0 kV. The turbo gas temperature was 325 ◦C and the CAD gas flow setting was medium. Curtain gas, GS1 and GS2 were 10, 20, and 0, respectively. The declustering potentials (DP), entrance potential (EP) and a collision exit potential (CXP) was 76, 10 and 14 V, respectively. The mass spectrometer was operated in MRM mode with collision energy (CE) of 20 V and 19 V for digoxin and digitoxin, respectively. The transitions (precursor to product) monitored was *m/z* 798→651 for digoxin, and m/z 782→365 for digitoxin (IS) in positive mode. The dwell time was set to 150 ms. Both Q1 and Q3 quadrupoles were maintained at unit resolution.

Propranolol. A stock solution of 20 µM of propranolol was prepared in 50/50 methanol:blank media. Each stock was combined in a ratio of 1:1 and serial dilutions were prepared to generate a standard curve. Ten µL of each standard or sample was mixed with 200 µL of the internal standard, metaprolol (1 µg/mL) prepared in methanol. 5 µL was injected for determination of propranolol concentration. LC–MS/MS analyses were performed using an Agilent 1200 HPLC system coupled to a PE Sciex API 4000 Qtrap tandem mass spectrometer with a Turbo Ionspray . The analytical column was a Phenomenex Synergi Max RP, 50 mm × 2.1 mm, 4 um and was kept at ambient temperature. Mobile phase A consisted of water with 5 mM ammonium formate (pH 3.4) and mobile phase B consisted of acetonitrile with 0.1% formic acid. The total run time was 5.5 min with an initial gradient of 2% mobile phase B. The initial conditions were held for 1 minute, followed by an increase to 95% B over 0.5 minutes. Mobile phase B was held at 95% B for 1.5 minute followed by re-equilibration to initial conditions for 2.5 minutes. The flow rate was set to 0.5 mL/minute. The Ionspray needle was maintained at 5.0 kV. The turbo gas temperature was 350 ◦C and the CAD gas flow setting was medium. Curtain gas, GS1 and GS2 were 10, 20, and 0, respectively. The declustering potentials (DP), entrance potential (EP) and a collision exit potential (CXP) was 60, 10 and 18 V, respectively. The mass spectrometer was operated in MRM mode with collision energy (CE) of 25 V for digoxin and digitoxin. The transitions (precursor to product) monitored was *m/z* 260→183 for propanolol, and m/z 268→191 for metoprolol (IS) in positive mode. The dwell time was set to 150 ms. Both Q1 and Q3 quadrupoles were maintained at unit resolution.

Toxicity testing

Bioprinted intestinal tissues were cultured as described until day ten. Baseline TEER of each sample was measured prior to treatment with indomethacin or TNFα. Tissues were treated with vehicle or test compound (indomethacin at 0.1-1 mM or 100 ng/mL TNFα) for 24 hours, then study media was collected and replaced with blank culture media before repeat TEER measurements. Tissues were collected for histology. Spent media collected from control or indomethacin treated tissues was

measured using a colorimetric assay for lactate dehydrogenase (LDH) per manufacturer's instructions. Prostaglandin E_2 was measured in spent media collected from control or indomethacin treated tissues by ELISA per manufacturer's instructions. Tissues treated with TNFα were collected for RNA isolation and gene expression analysis.

Statistical analysis

All data was analyzed using GraphPad Prism 6 software by t-test, one-way Anova, or two-way Anova as described in the text or figure legend. Data are presented as mean +/- standard deviation. The number of biological replicates, 'n', is noted in the figure or table legends.